Band mixing and ambipolar transport by surface acoustic waves in GaAs quantum wells

P. V. Santos,* F. Alsina, J. A. H. Stotz, and R. Hey
Paul-Drude-Institut für Festkörperelektronik, Hausvogteiplatz 5–7, 10117 Berlin, Germany

S. Eshlaghi and A. D. Wieck
Lehrstuhl für Angewandte Festkörperphysik, Ruhr-Universität Bochum, 44780 Bochum, Germany
(Received 22 October 2003; revised manuscript received 6 January 2004; published 20 April 2004)

The interaction of strong surface acoustic wave (SAW) fields with the electronic band structure of GaAs quantum wells (QW's) is investigated using spatially resolved photoluminescence (PL) spectroscopy. The optical studies are accompanied by $\mathbf{k}\cdot\mathbf{p}$ and tight-binding (TB) calculations of the SAW effects on the electronic band structure. The SAW induces a time-dependent coupling between the heavy- (hh) and light-hole (lh) states in the valence band of the QW's, which leads to an anticrossing of their energy levels for high SAW intensities. The coupling alters the strength and polarization of the optical transitions and can be reproduced by calculations of the optical transition matrix elements. Spatially resolved PL measurements of the SAW-induced ambipolar transport of electrons and holes provide evidence of a reduction of the transport efficiency for high SAW fields, which is attributed to a decrease of the hole mobility as the hh and lh levels approach each other. This conclusion is supported by TB calculations that show a significant enhancement of the heavy-hole effective mass under these conditions. In addition, the mobility may also be reduced by the squeezing of the wave functions towards the QW interfaces induced by strong piezoelectric fields, which makes the transport more sensitive to potential fluctuations induced by interface roughness and defects in the barrier layers.

DOI: 10.1103/PhysRevB.69.155318 PACS number(s): 77.65.Dq, 77.65.Ly, 78.20.Hp, 78.55.−m

I. INTRODUCTION

There has been considerable interest in recent years in the use of surface acoustic waves (SAW's) to modulate the in-plane electronic properties of quantum well (QW) structures.[1–3] These waves can be easily generated in piezoelectric materials (such as the III-V semiconductors) by means of interdigital transducers (IDT's) deposited on the sample surface, as illustrated in Fig. 1(a). When excited by a radio frequency (rf) voltage with frequency $f_{\mathrm{SAW}} = \omega_{\mathrm{SAW}}/2\pi$ typically from a few hundreds of MHz to a few GHz, the IDT launches a SAW with wavelength $\lambda_{\mathrm{SAW}} = v_{\mathrm{SAW}}/f_{\mathrm{SAW}}$ of the order of a micrometer, where v_{SAW} is the wave phase velocity ($v_{\mathrm{SAW}} = 2866$ m/s for GaAs). Furthermore, the SAW fields are concentrated within a thin surface layer with thickness comparable to λ_{SAW}, thus leading to high acoustic power densities. The dynamic character of the modulation, together with the absence of lateral interfaces in the modulated region, makes it an alternative to the static structuring methods achieved by conventional photo- and electron-beam lithography.

The influence of static strain on the band structure has been extensively investigated in bulk[4–6] as well as in superlattices of semiconducting materials.[7–9] The dynamic SAW strain has been shown to induce a small lateral type-I modulation of the electronic transition energies E_g [as indicated by $E_{g,\max}$ and $E_{g,\min}$ in Fig. 1(b)],[10,11] refractive index,[12] polarization,[10] and oscillator strength of optical transitions.[10,11] The modulation of the optical properties is the basis of operation of elasto-optic devices including Bragg cells[13,14] and optical switches.[15]

In a piezoelectric material, a SAW normally carries a piezoelectric potential Φ_{SAW} in addition to the strain field, and the type-II modulation induced by Φ_{SAW} interacts strongly with carriers in semiconducting materials. The dynamic nature of Φ_{SAW} has been used to transport carriers in two-dimensional electron gases.[2,16–18] More recently, it has been demonstrated that the piezoelectric field is sufficiently strong to ionize electron-hole pairs and transport the resulting free carriers, leading to the acoustically induced ambipolar transport (AIT) illustrated in Fig. 1(b). The electrons and holes are transported as charge packets stored in the maxima and minima, respectively, of the moving SAW potential.[2,10] The phase relationship between the type-II modulation by the piezoelectric potential and the type-I modulation induced by

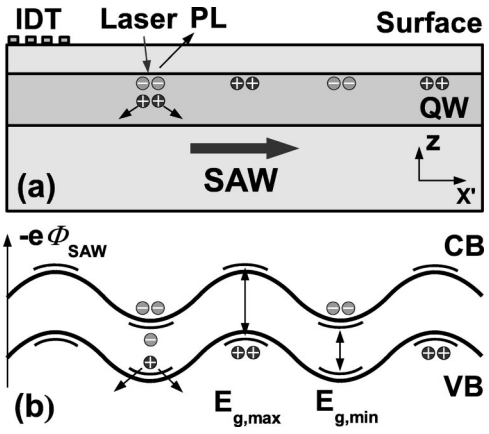

FIG. 1. Schematic representations of the (a) carrier transport by SAW's and (b) lateral modulation of the band edges by a SAW propagating along the $x' = [110]$ direction of the (001) GaAs surface. The SAW is generated by an interdigital transducer (IDT) deposited on the sample surface. The piezoelectric potential Φ_{SAW} creates a type-II modulation of the bands, which spatially separates photogenerated electrons and holes. The strain field modulates the band gap between the values $E_{g,\min}$ and $E_{g,\max}$.

the strain field produced by a SAW propagating along $x' = [110]$ as illustrated in Fig. 1(b). We remind ourselves that the modulation of the band gap by the strain field also induces a longitudinal force on the carriers proportional to $\partial E_g / \partial x'$, where x' denotes the SAW propagation direction. For SAW's in the frequency range below a few GHz, however, this force is much smaller than that due to the piezoelectric field. As a result, the SAW acoustic field normally plays a minor role in the AIT, which is therefore dominated by the piezoelectric effect.

In this paper, we report a detailed investigation of the interaction between photogenerated carriers and strong SAW fields in GaAs QW structures. The optical studies were performed using photoluminescence spectroscopy (PL) to detect the electronic transitions and the AIT resulting from the SAW and are accompanied by calculations of the effects of the strain and piezoelectric fields on the band structure using the tight-binding (TB) and the $\mathbf{k}\cdot\mathbf{p}$ methods. In a previous study, we have investigated the interaction between carriers and low-intensity SAW fields in GaAs QW's.[10] Here, we show that the strong SAW fields induce a time-dependent coupling between the heavy- (hh) and light-hole (lh) states in the valence band (VB) of the QW's. This coupling leads to an anticrossing of the hh-lh energy levels as they approach each other for high SAW intensities and also alters both the strength and the polarization of the optical transitions. In addition, the calculations show that the modifications in the VB structure caused by the hh-lh coupling induce an increase of the hh effective mass and, consequently, reduce the carrier mobility. In fact, spatially dependent PL studies of the ambipolar AIT show an unusual reduction of the transport efficiency at high SAW amplitudes, which is attributed to a decrease in the mobility of the holes. Two mechanisms are invoked to explain the mobility reduction: (i) the previously mentioned mixing of the hh and lh states and (ii) the squeezing of the electron and hole wave functions towards the QW interface by the vertical component F_z of the SAW piezoelectric field, which makes the transport more susceptible to potential fluctuations induced by interface roughness and defects in the barrier layers.

We start with a description of the QW samples and of the experimental techniques used to measure the PL under the influence of a SAW (Sec. II). The experimental results are presented in Sec. III, where we first analyze the effects of the SAW strain (Sec. III A) and piezoelectric fields (Sec. III B) on the PL, and then present results relative to AIT (Sec. III C). In Sec. IV, we introduce the TB procedure used to determine the electronic band structure followed by a comparison of the calculation with the experimental results. The main conclusions are summarized in Sec. V.

II. EXPERIMENTAL DETAILS

Three types of QW samples grown on GaAs (001) by molecular-beam epitaxy were investigated. Sample *A* contains three QW's ($QW_1 - QW_3$) with short-period (AlAs/GaAs) superlattice barriers. QW_1, QW_2, and QW_3 have thicknesses of 19.8, 15.4, and 12.2 nm, respectively, and are placed between 150 and 200 nm below the surface. Sample *B* also contains three QW's with the same thicknesses as in sample *A*, but placed at depths between 100 and 150 nm. Finally, sample *C* consists of a 12 nm thick single QW with $Al_{0.3}Ga_{0.7}As$ barriers placed 100 nm below the surface.

SAW's propagating along the $x' = [110]$ surface direction were generated by aluminum split-finger IDT's deposited on the sample surface. The IDT's were designed for operation at a wavelength λ_{SAW} of 5.6 μm, corresponding to a frequency $\omega_{SAW}/2\pi$ of 520 MHz at 15 K for sample *A*. In sample *B*, the SAW's were generated by focusing IDT's, which produce SAW fields up to five times larger than those generated by the conventional IDT's used in the other samples.[19]

For the optical measurements, the samples were mounted in a cryostat with special feed-throughs for the rf excitation of the acoustic transducers. Due to rf coupling losses, the acoustic SAW power is normally much smaller than the nominal rf-power supplied by the rf generator. The setup also allows for interferometric measurements of the vertical (i.e., parallel to z) surface displacement induced by the SAW, which was used to calculate the absolute magnitude of the SAW acoustic field. The latter will be specified in terms of the linear power density P_l defined as the acoustic power per unit length perpendicular to the SAW propagation direction.

The PL measurements were carried out at 15 K using a confocal microscope with illumination and detection areas with a diameter of ≈ 2 μm. The continuous radiation from a Ti:sapphire laser ($\lambda_L = 765$ nm) was employed as excitation source and polarized perpendicular to the SAW propagation direction (i.e., along $y' = [1\bar{1}0]$); the PL polarized either along or perpendicular to the x' direction was detected by a cooled charge coupled device (CCD) camera.

III. RESULTS

In order to distinguish between the effects of the strain and piezoelectric fields, the PL measurements were performed both on the free surface and underneath a semitransparent metal stripe evaporated on the SAW propagation path. Figure 2 displays the depth dependence of both the longitudinal ($F_{x'}$) and vertical (F_z) piezoelectric fields induced by a $\lambda_{SAW} = 5.6$ μm SAW on a free-surface region (solid lines) and underneath a metal layer (dashed lines) on a GaAs (001) substrate. The difference between the elastic properties of the thin $Al_{0.3}Ga_{0.7}As$ barrier layers and GaAs were neglected in these calculations. The vertical dashed lines mark the region where the QW's of sample *A* are placed. Because the metal stripe short-circuits the piezoelectric field,[2,10] the field amplitudes at the depth of the QW's are strongly reduced underneath the metal. In contrast, the strain field remains essentially unaffected by the thin metal stripe.[10] An alternative method to short-circuit the piezoelectric field is to perform the experiment under high optical excitation conditions. In this case, large numbers of photogenerated carriers are produced, and the screening field from the charged carriers is able to suppress the SAW piezoelectric field.

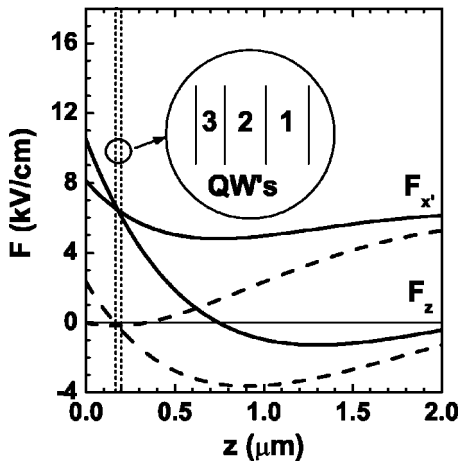

FIG. 2. Calculated depth profiles of the longitudinal ($F_{x'}$) and vertical (F_z) components of the piezoelectric field induced by a SAW with $P_l = 100$ W/m under the free surface (solid lines) and underneath the metal stripe (dashed lines). The vertical dashed lines show the position of the QW's for sample *A*.

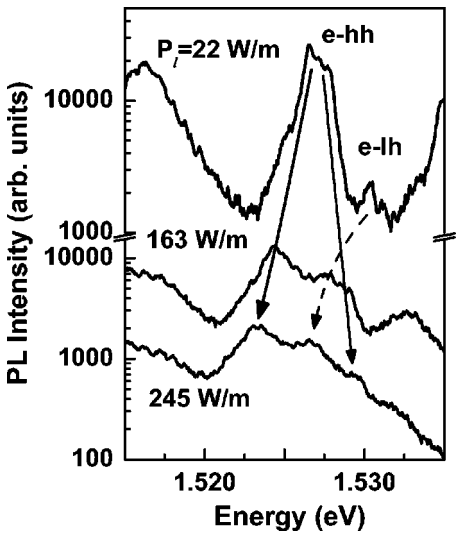

FIG. 4. Photoluminescence spectra of QW_1 of sample *B* at 15 K recorded on the free surface under a SAW with different power densities P_l. The solid (dashed) arrow guides the eye to identify features associated with *e*-hh (*e*-lh) transitions of QW_1.

A. Strain effects

Figures 3(a) and 3(b) display PL spectra recorded on sample *A* for different SAW amplitudes underneath the metal stripe and on the free surface, respectively. In the absence of a SAW (upper curves), the spectra are dominated by the emission from *e*-hh excitons in the QW's with weaker features associated with the *e*-lh transitions [indicated by the dashed lines in Fig. 3(a)].

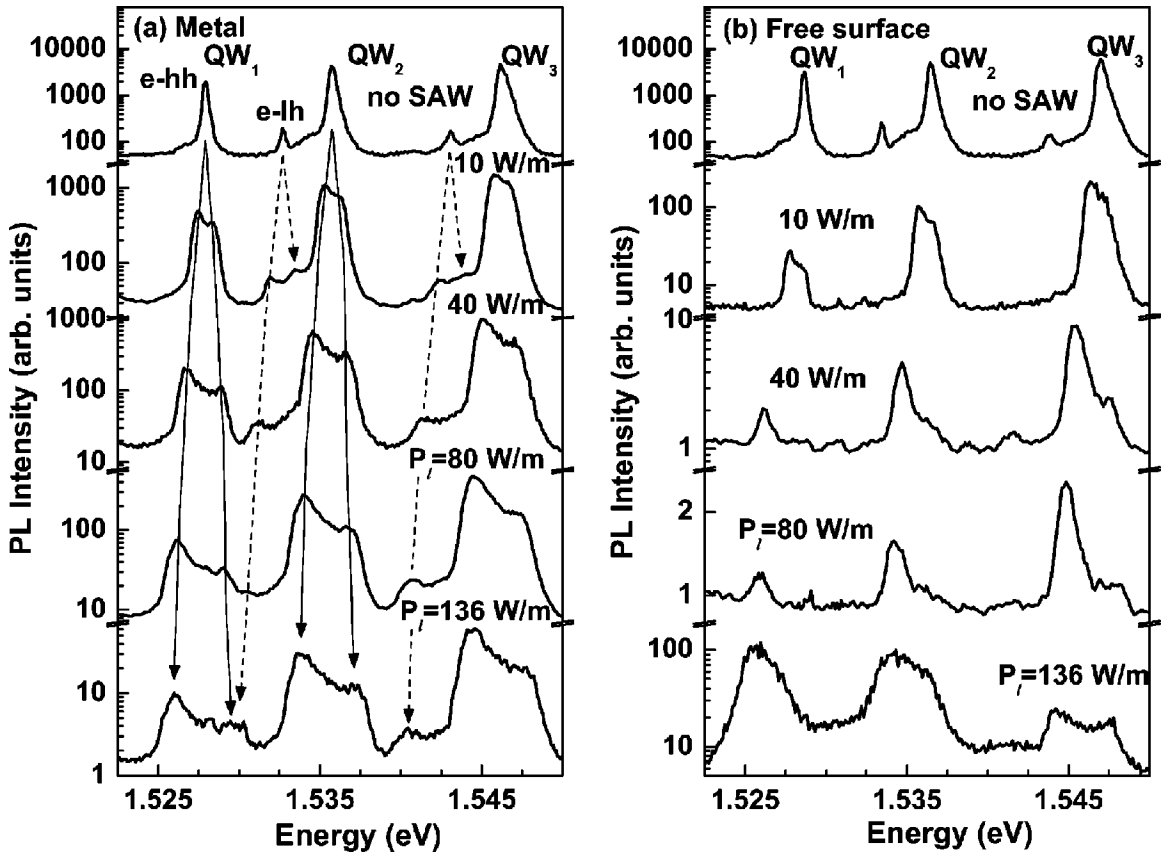

FIG. 3. Photoluminescence spectra of QW_1-QW_3 of sample *A* at 15 K recorded (a) over a semitransparent metal stripe and (b) on the free sample surface, in the absence of a SAW and under SAW's with different power densities P_l. The solid and dashed lines guide the eye to identify the features associated with *e*-hh and *e*-lh transitions of QW_1 and QW_2.

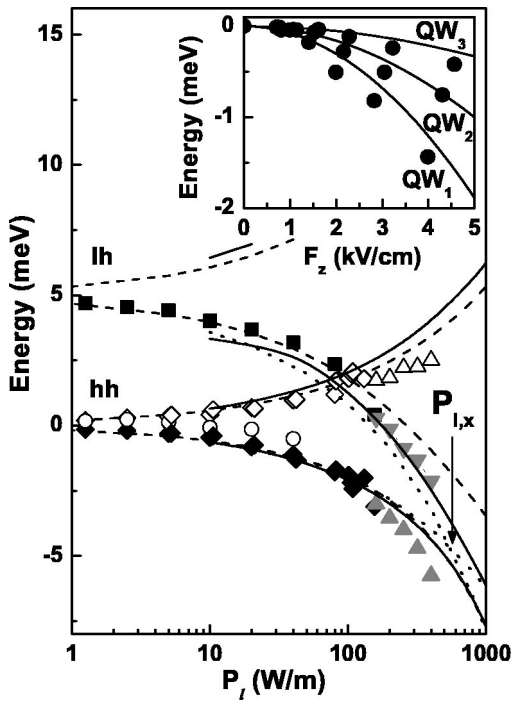

FIG. 5. Energy shifts relative to the hh transition of the hh-related (diamonds) and lh-related (squares) transitions for QW_1 of sample *A* as a function of the SAW power density P_l obtained from PL spectra recorded over the metal stripe. The normal and inverted triangles correspond, respectively, to the energies of the hh and lh transitions measured on the free surface of sample *B* under high optical excitation conditions, such that the local Φ_{SAW} is suppressed. The filled and empty symbols denote emission collected at the SAW phases of minimum and maximum band gaps, respectively. The solid and dashed lines reproduce the energies obtained from tight-binding and $\mathbf{k}\cdot\mathbf{p}$ calculations, respectively. The dotted lines schematically show the anticrossing position of the hh and lh transitions, which occurs for a SAW power $P_{l,x}\sim 600$ W/m. The circles denote the energies of the hh-related transitions measured on the free surface from QW_1 for a SAW propagating along the [110] direction. Inset: Average energy of the *e*-hh doublet for $QW_1 - QW_3$ as a function of the vertical component of the piezoelectric field. The lines correspond to calculations of the Stark shifts (see text for details).

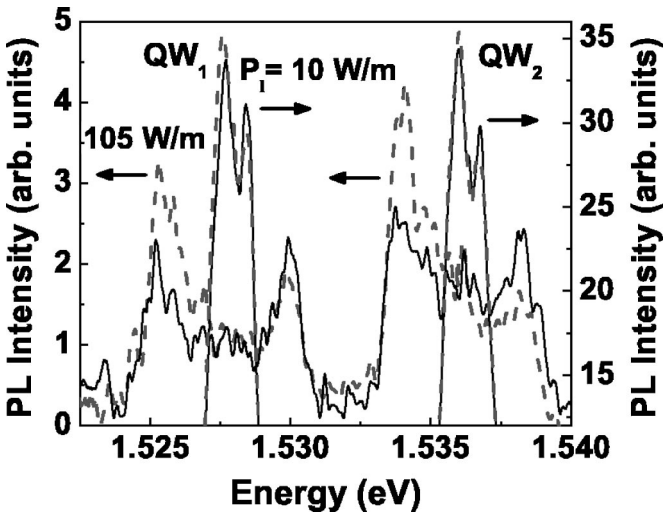

FIG. 6. Photoluminescence of QW_1 and QW_2 of sample *A* measured at 15 K on a semi-transparent metal stripe with SAW power densities P_l of 10 and 105 W/m. The spectra were recorded with polarization parallel (solid lines) and perpendicular (dashed lines) to the SAW propagation direction.

In this section, we concentrate on PL spectra collected underneath the metal stripe [Fig. 3(a)], which are mainly sensitive to the SAW strain field. With increasing SAW intensity, each PL line splits into a doublet due to the band-gap modulation induced by the strain.[10] As will be discussed in detail in Sec. IV B, the lower $[E_{\mathrm{hh(lh),min}}]$ and higher $[E_{\mathrm{hh(lh),max}}]$ energy components of the doublet correspond to the transition energies at the positions of maximum tensile and compressive strain, respectively. The PL appears as two distinct spectral lines instead of a single broadened line because of the sinusoidal character of the band-gap modulation. The latter subjects the material to longer periods of highly compressive (corresponding to a higher band gap) and highly extensive (corresponding to a smaller band gap) hydrostatic strain and shorter periods of low strain values. The splitting of the PL line results, therefore, from a larger time-averaged joint density of states at the positions of the minimum and maximum band gaps.[10,11]

The results from Fig. 3 for low SAW intensities are essentially similar to those reported in Ref. 10, where the maximum SAW power density did not exceed ≈ 20 W/m. The dependence of the energy splitting on SAW intensity is much larger for the *e*-lh transition than for the *e*-hh.[10] As a result, when the SAW amplitude increases, the lower-energy *e*-lh doublet component approaches the range of the *e*-hh transitions, as indicated by the dashed line for QW_1 in Fig. 3(a). This effect becomes evident for $P_l > 150$ W/m in Fig. 4, which shows PL spectra recorded on sample *B*. The measurements in this case were performed on the free surface using high illumination intensities. The high density of photogenerated carriers effectively screens the piezoelectric field—proven by the small degree of PL quenching. The modifications in the spectra are thus primarily associated with the SAW strain field. As will be discussed in detail below, the interaction of the low-energy *e*-hh and *e*-lh doublet component results in an anticrossing behavior as the two transitions converge for high acoustic powers.

High SAW amplitudes also change the relative intensities of the PL doublets. For low SAW amplitudes in Fig. 4, the oscillator strength is concentrated on the lower-energy doublet component. As the *e*-lh line, at the position of minimum gap, approaches and crosses the higher-energy *e*-hh transition, the ratio of the *e*-lh to the *e*-hh PL intensities suddenly increases, as demonstrated in Fig. 4. As will be shown in Sec. IV C, such a change in oscillator strength is expected in the anticrossing region.

The dependence of the transition energies of QW_1 of sample *A* on SAW power is summarized in Fig. 5. The diamonds and squares show the measured energy shifts (relative to the *e*-hh transition energy in the absence of a SAW) for the transitions involving the lowest and highest VB's, respectively, as a function of P_l. The data in the range of high

powers (triangles) were obtained from PL measurements performed on sample *B* under high illumination intensities. The solid and dashed lines in Fig. 5 reproduce calculations of the *e*-hh and *e*-lh transition energies performed following the procedures to be discussed in Sec. IV B. The filled and empty symbols denote emission collected for two distinct SAW phases $\phi_{SAW}=k_{SAW}x'-\omega_{SAW}t$, where $k_{SAW}=2\pi/\lambda_{SAW}$ is the SAW wave vector. An important point to note is that the hh and lh states of the same phase can interact with each other. This interaction becomes particularly strong at the phases corresponding to a minimum band gap, where the hh and lh energies approache each other. The interaction leads to the anticrossing behavior at the power density $P_{l,x}\sim 600$ W/m. The dotted lines in Fig. 5 show the expected behavior in the absence of hh-lh coupling (see Sec. IV for details). Although the SAW intensities achieved in the present experiments are below $P_{l,x}$, there are already considerable deviations from the expected power dependence for $P_l > 100$ W/m.

The integrated PL collected underneath the metal stripe remains independent of the SAW amplitude for $P_l < 10$ W/m. For higher SAW amplitudes, however, the PL intensity becomes strongly suppressed. Such a behavior has not been previously reported for measurements in QW's underneath a metal stripe:[10] it is attributed to the much higher SAW power densities (approximately one order of magnitude higher) used in the present case, which become sufficiently strong to transport carriers even when Φ_{SAW} becomes partially screened underneath the metal layer.

The SAW strain also leads to a polarization dependence of the emitted radiation.[10,12] This is apparent in Fig. 6, which displays the PL of sample *A* measured at 15 K for polarization parallel (thin lines) and perpendicular (thick lines) to the SAW propagation direction. The PL of the high-energy component of the *e*-hh doublet is preferentially polarized along the SAW propagation direction, while the low-energy component is polarized perpendicular to it. It is interesting to note that the polarization changes are very sensitive to the SAW amplitude, being observable even for low SAW intensities. As will be discussed in Sec. IV C, these changes arise from the mixing of the VB states induced by the SAW strain.

B. Piezoelectric effects

The contribution of the piezoelectric field becomes evident in the PL spectra recorded for low optical excitation outside the metal stripe [Fig. 3(b)], where the field is not susceptible to the screening by carriers in the semiconductor or in the metal layer. As with the experiments underneath the metal stripe, the PL lines from the free surface split with increasing SAW amplitude. While the PL splitting is comparable to that detected underneath the metal, the transition energies measured on the free surface are slightly redshifted. This redshift is attributed to the quantum-confined Stark effect (QCSE) associated with F_z [cf. Fig. 2]. In order to support this conclusion, the inset of Fig. 5 displays the average energy of the *e*-hh PL doublets as a function of F_z for the different QW's. The lines in the inset are the QCSE shifts calculated according to Ref. 20, which well reproduce the measured data. As expected from the QCSE, the energy shifts increase with increasing QW thickness.

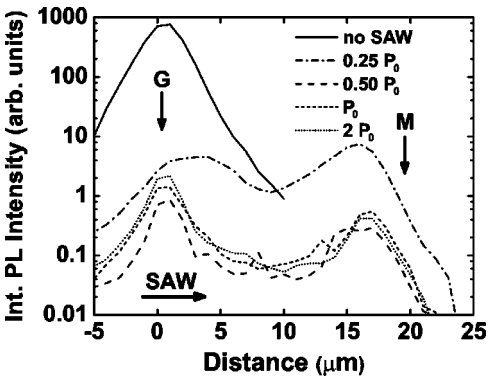

FIG. 7. Spatial profiles of the integrated PL intensity for sample *C* with different SAW power densities relative to the reference level P_0. The PL was excited by a focused laser spot at position *G*. The carriers are transported by the SAW until they recombine close to the position *M* at the edge of an opaque metal stripe, which is used to screen the piezoelectric field.

For SAW power densities between 10 and 100 W/m, the degree of PL quenching on the free surface is at least an order of magnitude higher than for measurements underneath the metal strip. As illustrated in Fig. 1(b), the suppression is related to (i) the ionization of the photoexcited excitons[1–3] and (ii) the sweep of the electron-hole pairs out of the PL detection spot by the field component $F_{x'}$.[3,10] The PL quenching for $P_l < 100$ W/m is accompanied by a strong transfer of oscillator strength to the lower energy component of the doublets, which is much more pronounced than in Fig. 3(a). For higher SAW powers, however, the oscillator strength close to the position of the higher doublet component increases [cf. Fig. 3(b)]. It is interesting to note that, in this regime, the spectral shape looks quite similar to that recorded underneath the metal stripe. Furthermore, within a narrow range of SAW power densities ($100\ \text{W/m} < P_l < 150$ W/m) the PL intensity shows a remarkable *increase* with SAW amplitude [note the different vertical scales in Fig. 3(b)] and even *exceeds* that detected under the metal. The degree of PL enhancement depends on the thickness of the QW and is accompanied by pronounced PL emission for energies in between the doublets, which is particularly strong for the wider QW's.

The PL enhancement described above has been observed neither in the emission line from the substrate nor in measurements underneath the metal stripe. We also observed that it disappears as the SAW excitation frequency is detuned from resonance in order to reduce the acoustic intensity. These observations, together with the dependence on QW thickness, indicate that it is a specific property of the QW structures and not related to heating effects due to the high SAW amplitudes. Moreover, we also found that the PL enhancement as a function of P_l depends on the level of light intensity, i.e., the effect is primarily of piezoelectric origin and becomes reduced when the piezoelectric field is screened by a high density of photogenerated carriers.

C. Transport efficiency

The PL enhancement for high SAW fields is accompanied by a reduction of the transport efficiency of electrons and holes by the SAW traveling fields (cf. Fig. 1). The latter was investigated by generating *e*-*h* pairs within a microscopic ($\ll\lambda_{SAW}$) illumination spot within the SAW path at a position denoted as *G* in Fig. 7. The electrons and holes are transported by the SAW until they recombine close to the edge *M* of an opaque metal stripe placed across the SAW propagation path 20 μm away from *G*.[2,21] Figure 7 displays spatial profiles of the integrated PL intensity along the transport path recorded for different SAW powers on sample *C*. In the absence of a SAW, the PL signal decays exponentially with distance from *G*, as expected for exciton diffusion (solid line). Note that the PL decay is, in this case, symmetric about the generation spot *G*.

Under a weak SAW ($P_l=0.25P_0$), the electrons and holes are transported by the SAW, as shown by the enhanced PL signal detected near *M* and by the strong suppression of the emission at *G*. As the SAW amplitude is further increased ($P_l=0.5P_0$), the piezoelectric field also becomes sufficiently strong to transport the carriers underneath the metal stripe, thus reducing the recombination near *M*. At the same time, the recombination maximum near the metal moves closer to *M*. For powers exceeding $0.5P_0$, no further changes are observed near *M*. In contrast, the PL increases at *G*, in agreement with the data in Fig. 3(b). The effect is attributed to a reduction of the transport efficiency for high SAW intensities induced by the vertical component of the piezoelectric field.

IV. DISCUSSION

The modifications to the band structure induced by the SAW occur on two length scales. The first is determined by the SAW wavelength, which is considerably larger than the lattice constant. The second is associated with changes of the lattice structure on the microscopic level induced by the SAW strain and piezoelectric fields. In order to take into account these two different length scales, the calculations of the effects of the SAW fields on the band structure were performed in two steps. First, the strain and piezoelectric fields induced by a SAW were determined by solving the equations for the propagation of acoustic waves in an elastic medium.[22] The strain and piezoelectric fields were then used to modify the local atomic positions in microscopic band structure calculations using the TB method. We also performed, for comparison, band structure calculations using the $\mathbf{k}\cdot\mathbf{p}$ method. These calculations included the interaction between the four highest VB's (including spin) and took into account the strain using the Hamiltonian from Bir and Pikus.[6,23] The $\mathbf{k}\cdot\mathbf{p}$ calculations presented here assume infinite barrier potentials and neglect the effects of the piezoelectric field. As a result, they cannot account for the band mixing induced by the penetration of the wave functions in the barrier layers or by the asymmetries introduced by the piezoelectric field. The confinement energies of the *e*, hh, and lh states at the Γ point in the absence of strain were used as an input to the $\mathbf{k}\cdot\mathbf{p}$ calculations.

A. Tight-binding calculations

The TB calculations of the QW band structure were performed using a periodic supercell containing the GaAs QW and the $Al_{0.3}Ga_{0.7}As$ barriers. Although computationally more cumbersome than macroscopic methods (such as the $\mathbf{k}\cdot\mathbf{p}$ calculations), the TB procedure can easily handle the effects of finite barrier heights, strain, and vertical electrical fields. The TB basis consists of ten sp^3s^* orbitals[24] per atom; the matrix elements between them includes only nearest-neighbor interactions. The spin-orbit coupling is accounted for using the formulation described in Refs. 25 and 26. Despite the simplicity, this orbital basis reproduces reasonably well the valence and the lowest conduction bands (CB's) of most bulk semiconductors.[24] The TB parameters for GaAs, which were extracted from Ref. 27, are well suited for the present investigations since they reproduce well the electron and the heavy-hole effective masses at the Γ point of bulk GaAs. The QW barriers were modeled by a $Al_{0.3}Ga_{0.7}As$ alloy with TB parameters interpolated from those of GaAs and AlAs.[28,35] The parameters for the As interface atoms were assumed to be an average between those in GaAs and $Al_{0.3}Ga_{0.7}As$. Finally, a VB offset of 0.16 eV was subtracted from the intra-atomic diagonal TB parameters of the $Al_{0.3}Ga_{0.7}As$ layers in order to reproduce the band discontinuity at the interfaces.

The positions of the atoms in the TB supercell were modified according to the local SAW strain field. The relative atomic positions within the distorted unit cell, however, are not unambiguously defined by the elasticity theory. These positions were calculated using the internal parameter.[29] The intersite TB parameters were corrected for the changes in the interatomic distances induced by the strain according to the power law

$$V_{ij}=V_{ij,0}\left(\frac{r}{r_0}\right)^{\alpha_{ij}}, \tag{1}$$

where V_{ij} with $i,j=s,p$ denotes the intersite TB parameters for *s*- and *p*-like orbitals (as defined in Ref. 30) and *r* is the anion-cation distance. The subscript 0 in V_{ij} and *r* is used to denote the equilibrium values for these quantities (i.e., in the absence of a strain). The simplest approximation consists of taking $\alpha_{ij}=2$.[31] We found, however, that while this approximation reproduces relatively well the strain dependence of the VB states, it strongly underestimates the hydrostatic deformation potential $a_{hyd}^{(CB)}$ of the lowest CB. In order to overcome this deficiency, we remember that in the nearest-neighbor TB approach used here, the CB energy at the Γ point is simply given by

$$E_{CB}=\frac{E_{s_1}+E_{s_2}}{2}+\frac{1}{2}\sqrt{D}, \tag{2}$$

where the E_{s_j}'s denote the on-site energy for anions ($j=1$) and cations ($j=2$) and $D=(E_{s_1}-E_{s_2})^2+4V_{xx}^2$. By taking the derivative of E_{CB} with respect to the *r*, one can show that α_{ss} is related to a_{hyd}^{CB} by

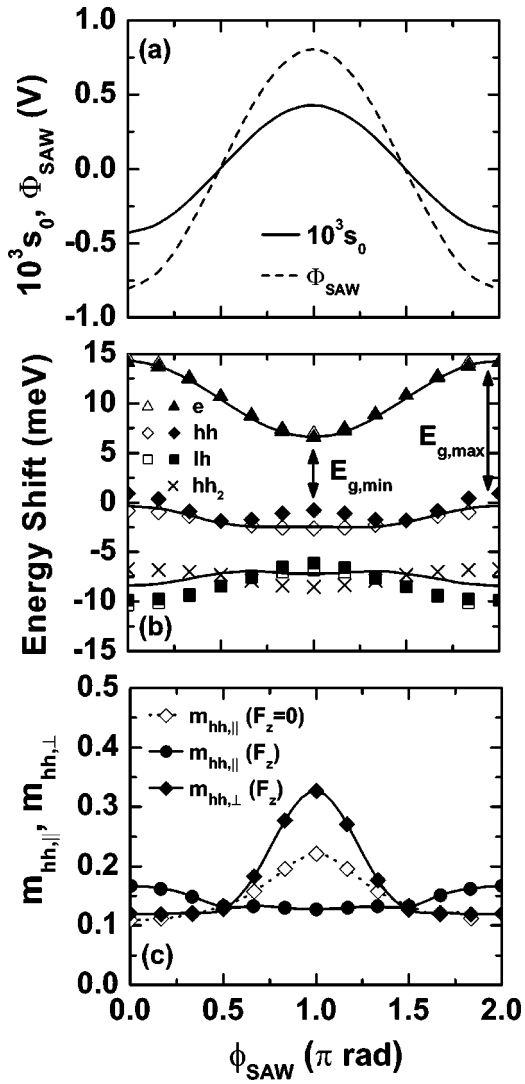

FIG. 8. Calculated dependence on the SAW phase ϕ_{SAW} of the: (a) hydrostatic strain s_0 (solid line) and piezoelectric potential Φ_{SAW} (dashed line), (b) lowest conduction band (e, triangles), highest heavy-hole (hh, diamonds) and light-hole (lh, squares) bands as well as the second heavy-hole band (hh_2, crosses) at the Γ point, as determined by TB calculations, and (c) effective hh masses parallel ($m_{\mathrm{hh},\|}$) and perpendicular ($m_{\mathrm{hh},\perp}$) to the SAW propagation direction. The solid lines in (b) represent the corresponding values obtained from a 4-band $\mathbf{k}\cdot\mathbf{p}$ calculation for the hh and lh levels. All energy shifts are relative to the band edges of bulk GaAs. The calculations were performed for a SAW propagating along the [110] direction with $P_l = 200$ W/m including [solid symbols in (b) and (c)] and neglecting (open symbols) the vertical component of the piezoelectric field F_z. Note that the CB energy shifts in (b) are practically independent of F_z.

$$a_{hyd}^{(CB)} = -\frac{2\alpha_{ss}}{3\sqrt{D}} V_{ss,0}. \tag{3}$$

A similar expression, with the subscripts s replaced by p, applies for the VB hydrostatic deformation potential. By using values from Ref. 23, we obtain $\alpha_{ss} = 4.57$ and $\alpha_{pp} = 2$ for GaAs. For the interaction between s and p orbitals, we used $\alpha_{sp} = (\alpha_{ss} + \alpha_{pp})/2$.

The effects of the vertical piezoelectric field component F_z were included by changing the on-site TB parameters following the procedure described in Ref. 32. Due to the large SAW periods, the effects of the longitudinal field cannot be taken into account by the microscopic TB method. In this case, the TB calculations were used to determine the wave-vector dispersion of the energy bands close to the Γ point. From the dispersion, the effective mass was then determined for different SAW phases.

The TB calculations were performed for a QW with the same thickness as QW_1 in samples *A* and *B*. Due to the small hh-lh splitting, this QW exhibits the strongest SAW-induced coupling between these levels for the SAW power densities used in the experiments. In the supercell calculations, the GaAs layers were assumed to have a thickness of 140 monolayers (19.8 nm) and to be spaced by 32-monolayer-thick (4.53 nm) $\mathrm{Al}_{0.3}\mathrm{Ga}_{0.7}\mathrm{As}$ layers. As in the experiments, the SAW was assumed to propagate along the [110] direction of the (001) GaAs surface.

B. Strain-induced effects: Transition energies

In this section, we discuss the effects of SAW strain on the band structure, which determines the transition energies in PL experiments underneath the metal stripe [cf. Fig. 3(a)]. The effects of the piezoelectric field, which were not included in the calculations presented here, will be addressed in Sec. IV D.

The SAW strain field possesses three nonvanishing strain components $\epsilon_{x'x'}$, ϵ_{zz}, and $\epsilon_{x'z}$ in the reference frame with main crystal axes $x' = [110]$, $y' = [1\bar{1}0]$, and $z = [001]$. The dependence of the hydrostatic component $s_0 = \epsilon_{x'x'} + \epsilon_{zz}$ calculated using the elastic model for SAW propagation is illustrated in Fig. 8(a). The lateral variation of the SAW strain field leads to a dependence of the band edges on the SAW phase ϕ_{SAW} or, equivalently, on position x' in the QW plane. The open symbols in Fig. 8(b) display the strain-induced modulation of the lowest CB (e) and of the three highest VB's (hh, lh, and hh_2) at the Γ point under a SAW with $P_l = 200$ W/m as a function of ϕ_{SAW}. The strain mixes hh and lh states. Here, the VB's are denoted according to their dominating character determined from the symmetry of the TB wave functions as hh (diamonds), lh (squares), and hh_2 (crosses, corresponding to the second hh state). The solid lines represent, for comparison, the corresponding VB energies (hh and lh) obtained from the $\mathbf{k}\cdot\mathbf{p}$ calculations. The two calculation methods yield comparable results for both the CB and the hh states, but small differences are observed for the lh states.

The modulation of the electronic VB$\rightarrow$CB transition energies is dominated by the shifts of the CB induced by the hydrostatic component s_0. The CB minimum (maximum) as well as the minimum (maximum) band gap occur for a SAW phase $\phi_{\mathrm{SAW}} = \pi$ rad ($\phi_{\mathrm{SAW}} = 0$ rad), where s_0 reaches its maximum (minimum) value. The shear component $\epsilon_{x'z}$ vanishes at these phases. The strain field then consists only of a tensile (compressive) component $\epsilon_{x'x'}$ along the x' direction plus a smaller compressive (tensile) component ϵ_{zz} along the z direction.

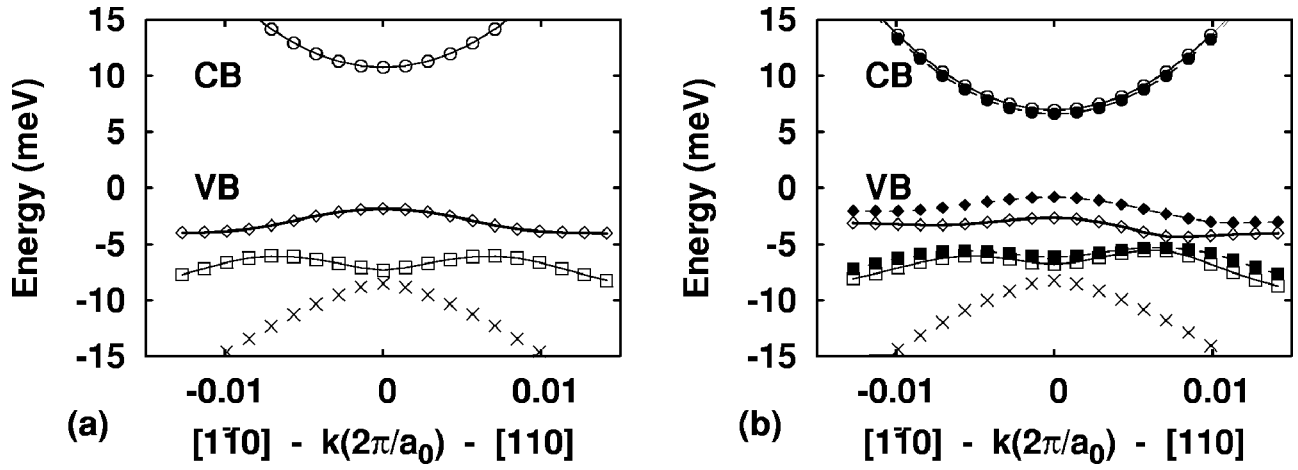

FIG. 9. Calculated in-plane electronic dispersion of QW_1 along the directions $[0\bar{1}0]\rightarrow\Gamma\rightarrow[110]$ (a) in the absence and (b) under a SAW with $P_l=200$ W/m. The electronic wave vector $\mathbf{k}$ is specified in units of $2\pi/a_0$, where a_0 is the GaAs lattice constant. The conduction band (CB) states are indicated by circles. The valence band (VB) states are denoted according to their dominant character at the Γ point by diamonds (hh-like), squares (lh-like), and crosses (hh_2-like). The symbols in (b) were calculated including (solid symbols) and neglecting (open symbols) the effects of the vertical component of the piezoelectric field F_z. All energies are relative to the band edges of bulk GaAs.

The hydrostatic deformation potential of the VB is much smaller than that of the CB.[23] The modifications of the VB are primarily determined by the mixing of states induced by the uniaxial strain component $s_u=\epsilon_{x'x'}-\epsilon_{zz}$. For the SAW amplitude $P_l=200$ W/m in Fig. 8, the highest VB has a predominantly hh character. The first lh and the second hh (hh_2) are strongly mixed in this QW (see discussion below). The second VB is predominantly of lh character at the position of minimum gap ($E_{g,\min}$), but away from this point, it becomes hh_2-like [crosses in Fig. 8(b)]. For higher SAW amplitudes, however, the relative positions of the first hh and lh levels may change.

The dependence of the transition energies at the Γ point on SAW amplitude is compared to the experimental data in Fig. 5 (lines). The solid and dashed lines were obtained from TB and $\mathbf{k}\cdot\mathbf{p}$ calculations, respectively. The $\mathbf{k}\cdot\mathbf{p}$ calculations well reproduce the measured data. The TB calculations overestimate the lh energy level in the absence of a SAW by approximately 1.5 meV. To allow for a better comparison with the experimental data, this energy shift was subtracted from the TB *e*-lh transition energies in Fig. 5. The calculations show the reduction of the *e*-hh and *e*-lh energy splitting and the anticrossing behavior at the position of minimum gap. The faster reduction of the *e*-lh energy reflects the well-documented upward shift of the lh states for a negative uniaxial strain s_u along the QW axis.[8] In order to estimate the anticrossing energy, the dotted lines were obtained by reflecting the upper hh and lh branches along a horizontal line passing through the energy of these states in the absence of a SAW. Since the modes of the upper branch do not interact with each other, the dotted lines approximate the power dependence in the absence of a hh-lh coupling and cross for $P_{l,x}\sim 600$ W/m. For higher power densities, the upper VB at the Γ point becomes predominantly of lh character.

The SAW strain also modifies the transition energies away from the Γ point. The open symbols in Figs. 9(a) and 9(b) compare the dispersion of the lowest CB (dots) and of the three highest VB's of QW_1 along the line $[0\bar{1}0]\rightarrow\Gamma\rightarrow[110]$ in the absence of a SAW and for a SAW with $P_l=200$ W/m, respectively. As in Fig. 8, the bands are denoted according to their predominant character as hh-like (dia-

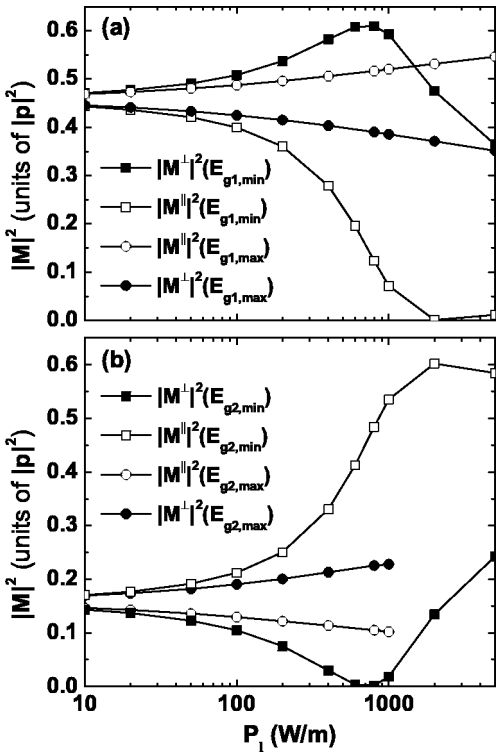

FIG. 10. Dependence of the optical transition matrix elements $|M|^2$ (in units of $|\mathbf{p}|^2=|\langle s|\mathbf{p}|p\rangle|^2$) for transitions from the CB to the (a) first and (b) second VB's on the linear power density P_l for SAW's propagating along the [110] direction. Calculations are shown for transitions at SAW phases of $\phi_{\mathrm{SAW}}=\pi$ (circles) and 0 rad (squares) for polarizations parallel (open symbols) and perpendicular (filled symbols) to the SAW propagation direction.

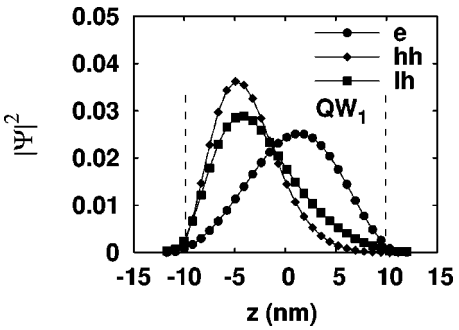

FIG. 11. Wave-function amplitudes ($|\Psi|^2$) for electrons (e, dots), hh (diamonds), and lh (squares) states in QW_1 at the SAW phase of minimum gap ($\phi_{SAW}=\pi$ rad) for $P_l=200$ W/m. The vertical dashed lines indicate the position of the interfaces between the QW and the $Al_{0.3}Ga_{0.7}As$ barriers. $z=10$ nm corresponds to the position of the upper QW interface.

monds), lh-like (squares), and hh_2-like (crosses). We note, however, that the lh and hh_2 states interact strongly for the given QW thickness.[27,33] The lh-hh_2 interaction is partially responsible for the upward dispersion of the lh level away from the Γ point. The bands under a SAW in Fig. 9(b) were calculated at the phase of maximum tensile strain [i.e., for $\phi_{SAW}=\pi$ rad in Fig. 8(b)] neglecting (open symbols) and including (solid symbols) the effects of the vertical piezoelectric field component F_z (see Sec. IV D).

As in Fig. 8, the primary modification induced by the strain in Fig. 9(b) is a downward shift of the CB. A closer analysis of the dispersion also shows that the mixing of the VB's under the SAW fields flattens the hh dispersion close to Γ along the [110] **k** direction and, therefore, increases the effective heavy-hole mass m^*_{hh}. This effect is quantified by the open diamonds in Fig. 8(c), which displays the phase dependence of m^*_{hh} for transport along the propagation direction for $P_l=200$ W/m. As expected, the maximum m^* occurs for $\phi_{SAW}=\pi$ rad, where the hh-lh mixing is the strongest. For high SAW amplitudes (close to $P_{l,x}\approx 600$ W/m), the calculations indicate a reversal in sign of the effective mass at the Γ point (not shown here). As a result, the VB maximum shifts to a **k** vector away from the zone center.[9] Due to the stronger dispersion of the CB, however, the maximum and minimum transition energies remain at Γ for the entire range of SAW power levels used in the experiments presented here.

C. Oscillator strength

The experimental data in Figs. 3(a) and 4 show, in addition to the energy splittings, significant changes in the relative intensities of the optical transitions with increasing SAW amplitude. In order to understand these variations, we have used the TB method to calculate the dependence of the optical transition matrix elements M on SAW strain.

Figures 10(a) and 10(b) display the matrix elements $|M|^2$ at the Γ point for the lowest transition energies E_{g1} and E_{g2}, respectively, as a function of P_l (due to the very small transition matrix elements, transitions to the CB involving the hh_2 band were not considered). $|M|^2$ is specified in units of the squared matrix element $|\mathbf{p}|^2$ of the momentum operator $\mathbf{p}$ between s and p orbitals in GaAs given by $|\langle s|\mathbf{p}|p\rangle|^2$. Calculations are presented for polarization parallel ($\|$) and perpendicular ($\perp$) to the SAW propagation direction. The subscripts min and max denote transitions at SAW phases of π and 0 rad corresponding, respectively, to the minimum and maximum values of the band gap.

For low SAW amplitudes, E_{g1} [Fig. 10(a)] and E_{g2} [Fig. 10(b)] correspond to the e-hh and e-lh transitions, respectively. The calculations, in this case, approach the expected ratio of 3:1 between the $|M|^2$ values for the e-hh and e-lh transitions in bulk GaAs. With increasing SAW intensity, the interaction between the hh and lh levels at the position of minimum gap [indicated by the squares in Figs. 10(a) and 10(b)] induces a transfer of oscillator strength between them. In order to compare the calculated oscillator strengths with the experimental results of Fig. 6 (and also of Fig. 4), we are first reminded that these PL measurements detect the emission with polarization along the SAW propagation direction (x' direction). In agreement with Fig. 10(a), the lowest energy transition for each QW in Fig. 6 (corresponding to $E_{g1,min}$) becomes preferentially polarized in the perpendicular direction as the SAW power increases. The opposite polarization is observed for the second transition ($E_{g1,max}$). Note that the SAW induces significant polarization changes even for relatively weak acoustic amplitudes. This behavior results from the linear dependence of the polarization on the hh-lh coupling, which contrasts with the quadratic dependence of the energy shifts as a function of SAW intensity.

The interaction between the hh and lh levels is maximal at the anticrossing power ($P_{l,x}\sim 600$ W/m), where the oscillator strength and polarization of $E_{g1,min}$ and $E_{g2,min}$ approach each other [indicated by the squares in Figs. 10(a) and 10(b)]. The behavior close to the anticrossing point is reproduced in the PL spectra recorded for high acoustic powers in Fig. 4, which shows that the lowest e-lh transition gains oscillator strength as the lh level approaches the hh level. Above the anticrossing power, the $E_{g1,min}$ level becomes predominantly lh-like.

D. Transport properties

In this section, we consider the modifications of the band structure induced by F_z and $F_{x'}$. Before proceeding to the energy shifts induced by F_z, we briefly discuss the modifications introduced by this field on the electronic wave functions. The latter are illustrated in Fig. 11 as calculated for the phase $\phi_{SAW}=\pi$ rad and a SAW power of $P_l=200$ W/m. F_z shifts the electron and hole wave functions towards opposite QW interfaces with several consequences. First, it changes the energy, dispersion, and the coupling of the electronic states as will be discussed in detail below. Second, it reduces the optical matrix elements between conduction and valence states as the electron and hole charge densities become spatially separated along z. Finally, the combined charge separation by F_z and $F_{x'}$, which are displaced in phase by 90° with respect to each other, leads to the SAW-induced transport pattern displayed in Fig. 1(a). Note that according to Fig. 11 (calculated for the phase $\phi_{SAW}=\pi$ rad), the elec-

trons are transported as charge packets squeezed against the upper QW interface. Due to the phase shift of approximately π between the electron and hole packets, the holes are also transported along the upper interface. The proximity of the transport path to the interface is expected to affect the transport efficiency since the carriers become more susceptible to scattering by potential fluctuations and defects at the interface or in the barriers.

The modification of the energy levels induced by F_z is shown by the solid symbols in Figs. 8 and 9(b). The most apparent effect is a reduction of the *e*-hh and, to a lesser extent, the *e*-lh transition energies induced by the QCSE. The shifts are primarily caused by an increase of the VB energy levels, which are more pronounced than those of the CB due to the larger hole effective mass. The larger hole mass also leads to a more pronounced squeezing of the VB wave functions towards the QW interfaces (cf. Fig. 11). Since the energy shifts associated with the QCSE are quadratic in F_z, the band gap is reduced both at the SAW phases of maximum compressive and tensile strain [cf. Fig. 8(b), corresponding to the maximum and minimum band gaps, respectively]. As a result, the QCSE redshifts both components (and therefore their average energy) of the strain-induced PL doublet by the same amount as illustrated by the solid symbols in the inset of Fig. 5.

The vertical field also increases the hh effective mass along the SAW propagation direction at the position of minimum gap. This effect is evident by the flattening of the hh dispersion along the [110] direction in Fig. 9(b) and quantified in Fig. 8(c), which compares the effective mass determined neglecting (open diamonds) and including (solid diamonds) F_z in the calculations. TB calculations performed inverting the field direction yield approximately the same levels of mass enhancement, thus indicating that, as for the Stark shifts, the field-induced mechanisms is quadratic in F_z. It is also interesting to note that the hh mass becomes large even though the splitting between the hh-like and lh-like levels close to Γ increases with F_z [cf. Fig. 9(b)]. While further investigations are required to determine the precise mechanism for the field-induced mass enhancement, we speculate that it is due to a stronger coupling between the hh and the hh_2 and lh levels in the asymmetric potential profile induced by F_z.

Based on the previous discussion, we propose the following model for the evolution of the PL spectrum (on the free surface) with increasing SAW amplitudes [cf. Fig. 3(b)]. For SAW power densities $P_l < 100$ W/m, the carrier distribution within the SAW potential and recombination dynamics are determined primarily by $F_{x'}$. For SAW's propagating along the [110] direction, preferential recombination takes place at the SAW phases corresponding to the minimum band gap. This behavior, which has been discussed in detail in Refs. 11 and 34, is associated with the lower mobility of the holes as compared to the electrons. The piezoelectric potential Φ_{SAW} concentrates the electrons and holes near the positions of minimum and maximum band gap, respectively [cf. Fig. 8]. When carriers are generated close to the positions of maximum gap, the highly mobile electrons are quickly extracted by the piezoelectric field, thus leading to a weak PL. In contrast, when the generation takes place close to the positions of minimum gap, the lower hole mobility prevents an effective carrier separation. Consequently, the intensity of the lower energy doublet component is expected to exceed the higher energy one, in agreement with Fig. 3(b).

The role of the vertical field F_z becomes important when the SAW power density exceeds 100 W/m. The larger band masses and the squeezing of the wave functions towards the upper QW interface lead to a reduction of the effective hole mobility. As a result, the PL at the generation point increases as the carriers are not efficiently separated [cf. Fig. 3(b)] while the transport efficiency reduces [cf. Fig. 7]. For SAW's propagating along the [110] direction, the larger effective mass primarily affects the AIT transport by reducing the ionization efficiency of electron-hole pair photogenerated close to the phases of minimum gap. The ionization at these positions, where the hole mobility is low, rely on the drift of the holes to the locations of minimum piezoelectric potential and maximum gap [cf. Fig. 1(b)]. In subsequent transport, the holes are captured at the phases of larger band gap, where no mass enhancement occurs. We note that a different behavior is expected for SAW's propagating along the $[1\bar{1}0]$ direction, where the holes are transported close to the SAW phases of minimum gap.[34]

The PL enhancement with increasing SAW amplitudes occurs only within a narrow range of SAW powers. For higher powers, the reduced overlap between the electron and hole wave functions shown in Fig. 11 prevents carrier recombination at the position of minimum and maximum gap, where F_z peaks. The recombination then takes place preferentially at the phases where F_z vanishes, thus leading to considerable PL emission at energies in between the strain-split doublets [compare the lowest curves in Figs. 3(a) and 3(b)]. This effect is pronounced for wider QW's, where F_z is more effective in separating the electron and hole charge densities, in agreement with the lowest spectrum in Fig. 3(b).

The longitudinal field $F_{x'}$ plays the primary role in the transport properties by SAW's as it is this sinusoidal modulation that carries the electrons and holes along the SAW propagation direction. Furthermore, we have showed in this paper that the strain field and the vertical component of the piezoelectric field F_z do significantly alter the energy levels within the QW so that their influence on the AIT cannot be neglected. Most surprisingly, under certain conditions F_z plays a fundamental role in the transport dynamics. In fact, the lowest curves in Figs. 3(a) and 3(b) show that, for $P_l > 100$ W/m, the carrier transport, as estimated from the degree of PL quenching, can be more efficient for a small F_z (underneath the metal, where the piezoelectric field is partially screened) than for the larger F_z values near the free surface. Since the strain field is approximately the same under the two conditions (and smaller values of $F_{x'}$ are always expected to reduce the transport), we conclude that the role of the vertical piezoelectric field clearly dominates over that of the strain field in determining the transport efficiency. Finally, the large influence of F_z on the transport properties may be associated not only with the reduced band mobility but also with the squeezing of the electronic wave functions

towards the upper QW interface, which makes the transport more sensitive to potential fluctuations and defects in the barrier layers. We note, however, that these detrimental effects can be eliminated by placing the transport path near a node of F_z. In fact, Fig. 2 shows that the vertical field F_z induced by a 5.6 μm SAW in GaAs vanishes at a depth of approximately 750 nm, where the longitudinal field $F_{x'}$ is comparable to the value near the surface. These proposals for the improvement of the transport efficiency are presently under investigation.

V. CONCLUSIONS

We have investigated the effects of intense SAW's on the band structure of GaAs QW's using spatially resolved PL spectroscopy. The SAW fields induce a dynamic coupling between the VB states with important consequences for the optical and transport properties. The coupling changes the oscillator strength and the polarization of the PL lines and it leads to an anticrossing of the hh-lh levels, as their energies converge for high acoustic fields.

Strong SAW fields reduce the efficiency of the acoustically induced transport of photogenerated carriers, which is attributed to a reduction of the hole mobility induced by the VB mixing. This result is supported by calculations of the effects of the SAW fields on the band structure, which predict an enhanced heavy-hole mass close to the hh-lh anticrossing. In addition to this mechanism, the mobility may also be affected by squeezing of the electronic wave functions towards the QW interface due to vertical field F_z, where the transport becomes more susceptible to potential fluctuations and defects at the interface or in the QW barrier layers. While the first mechanism is intrinsic, since it is associated with modifications in the band structure, the second one depends on the quality of the interfaces and can be minimized by improving the deposition techniques or by an appropriate placement of the transport path. Further investigations are required to clarify to what extent this mechanism affects the ambipolar transport.

ACKNOWLEDGMENTS

We thank H. T. Grahn for comments and for a critical reading of the manuscript. Support from the Deutsche Forschungsgemeinschaft (Projects Nos. SA598/2-1, GRK384, and SFB491) is gratefully acknowledged.

*Email address: santos@pdi-berlin.de

[1] K.S. Zhuravlev, D.P. Petrov, Y.B. Bolkhovityanov, and N.S. Rudaja, Appl. Phys. Lett. **70**, 3389 (1997).
[2] C. Rocke, S. Zimmermann, A. Wixforth, J.P. Kotthaus, G. Böhm, and G. Weimann, Phys. Rev. Lett. **78**, 4099 (1997).
[3] P.V. Santos, M. Ramsteiner, and F. Jungnickel, Appl. Phys. Lett. **72**, 2099 (1998).
[4] M. Cardona, *Modulation Spectroscopy* (Academic Press, New York, 1969).
[5] F.H. Pollak, Surf. Sci. **37**, 863 (1973).
[6] G.L. Bir and G.E. Pikus, *Symmetry and Strain-Induced Effects in Semiconductors* (Wiley, New York, 1974).
[7] H. Qiang, F.H. Pollak, K. Shum, Y. Takiguchi, R.R. Alfano, S.F. Fang, and H. Morkoç, Philos. Mag. B **70**, 381 (1994).
[8] P. Etchegoin, A. Fainstein, A.A. Sirenko, B. Koopmans, B. Richards, P.V. Santos, M. Cardona, K. Totenmeyer, and K. Eberl, Phys. Rev. B **53**, 13662 (1996).
[9] H.A.P. Tudury, M.K.K. Nakaema, F. Iikawa, J.A. Brum, E. Ribeiro, W. Carvalho, Jr., A.A. Bernussi, and A.L. Gobbi, Phys. Rev. B **64**, 153301 (2001).
[10] T. Sogawa, P.V. Santos, S.K. Zhang, S. Eshlaghi, A.D. Wieck, and K.H. Ploog, Phys. Rev. B **63**, 121307(R) (2001).
[11] F. Alsina, P.V. Santos, R. Hey, A. García-Cristóbal, and A. Cantarero, Phys. Rev. B **64**, 041304(R) (2001).
[12] P.V. Santos, Appl. Phys. Lett. **74**, 4002 (1999).
[13] A. Korpel, *Acousto-Optics* (Dekker, New York, 1997).
[14] P.V. Santos, J. Appl. Phys. **89**, 5060 (2001).
[15] M.M. de Lima, Jr., P.V. Santos, R. Hey, and S. Krishnamurthy, Physica E **21**, 809 (2004).
[16] W.J. Tanski, S.W. Merritt, R.N. Sacks, D.E. Cullen, E.J. Branciforte, R.D. Carroll, and T.C. Eschrich, Appl. Phys. Lett. **52**, 18 (1987).
[17] J.M. Shilton, V.I. Talyanskii, M. Pepper, D.A. Ritchie, J.E.F. Frost, C.J.B. Ford, C.G. Smith, and G.A.C. Jones, J. Phys.: Condens. Matter **8**, L531 (1996).
[18] M. Rotter, A.V. Kalameitsev, A.O. Govorov, W. Ruile, and A. Wixforth, Phys. Rev. Lett. **82**, 2171 (1999).
[19] M.M. de Lima, Jr., F. Alsina, W. Seidel, and P.V. Santos, J. Appl. Phys. **94**, 7848 (2003).
[20] G. Bastard, E.E. Mendez, L.L. Chang, and L. Esaki, Phys. Rev. B **28**, 3241 (1983).
[21] T. Sogawa, P.V. Santos, S.K. Zhang, S. Eshlaghi, A.D. Wieck, and K.H. Ploog, Phys. Rev. Lett. **87**, 276601 (2001).
[22] Y. Takagaki, E. Wiebicke, P.V. Santos, R. Hey, and K.H. Ploog, Semicond. Sci. Technol. **17**, 1008 (2002).
[23] P. Yu and M. Cardona, *Fundamentals of Semiconductors: Physics and Materials Properties* (Springer, Heidelberg, 1995).
[24] P. Vogl, H. Hjalmarson, and J. Dow, J. Phys. Chem. Solids **44**, 365 (1983).
[25] K.C. Hass, H. Ehrenreich, and B. Velicky, Phys. Rev. B **27**, 1088 (1983).
[26] D.J. Chadi, Phys. Rev. B **16**, 790 (1977).
[27] J.N. Schulman and Y.-C. Chang, Phys. Rev. B **31**, 2056 (1985).
[28] D.A. Contreras-Solorio, V.R. Velasco, and F. García-Moliner, Phys. Rev. B **47**, 4651 (1993).
[29] P.N. Keating, Phys. Rev. **145**, 1637 (1966).
[30] P.V. Santos, M. Willatzen, M. Cardona, and A. Cantarero, Phys. Rev. B **51**, 5121 (1995).
[31] W. A. Harrison, *Electronic Structure and the Properties of Solids* (Dover, New York, 1989).
[32] M. Graf and P. Vogl, Phys. Rev. B **51**, 4940 (1995).
[33] Y.-C. Chang and J.N. Schulman, Phys. Rev. B **31**, 2069 (1985).
[34] F. Alsina, P.V. Santos, and R. Hey, Phys. Rev. B **65**, 193301 (2002).
[35] We did not use the AlAs parameters from the same reference as for GaAs (Ref. 27) because they underestimate the CB *X* point energy of the AlAs layers, which in a superlattice becomes very close in energy to the GaAs-like first CB at the Γ point.